LNF–97/034

Tetragonal–Strain–Induced Local Structural Modifications in $InAs_xP_{1-x}$/InP Superlattices: a Detailed X–Ray–Absorption Investigation

S. Pascarelli, F. Boscherini, C. Lamberti, S. Mobilio

Physical Review B 56, 4, 1936–1947, (1997)

Tetragonal-strain-induced local structural modifications in $InAs_xP_{1-x}/InP$ superlattices: A detailed x-ray-absorption investigation

S. Pascarelli*
Istituto Nazionale per la Fisica della Materia, Via dell'Acciaio 139, 16152 Genova, Italy

F. Boscherini
Istituto Nazionale di Fisica Nucleare, Laboratori Nazionali di Frascati, P. O. Box 13, 00044 Frascati, Italy

C. Lamberti
Dipartimento di Chimica Inorganica, Fisica e dei Materiali, Università di Torino, Via P. Giuria 7, 10148 Torino, Italy

S. Mobilio
Dipartimento di Fisica, Università "Roma Tre," Via della Vasca Navale 84, 00146 Roma, Italy
and Istituto Nazionale di Fisica Nucleare, Laboratori Nazionali di Frascati, P. O. Box 13, 00044 Frascati, Italy
(Received 18 February 1997; revised manuscript received 10 April 1997)

We report a comprehensive investigation of the local structure around As in thin $InAs_xP_{1-x}$ strained layers in $InAs_xP_{1-x}/InP$ superlattices by fluorescence-detected x-ray-absorption fine structure; seven superlattice samples are studied as a function of composition, and compared to six unstrained, bulk samples of similar composition. Contributions up to the third coordination shell around As are clearly visible in the spectra, and are analyzed taking into account important multiple-scattering contributions. Results show that structural modifications due to tetragonal distortion appear mainly in the second and third coordination shells, while nearest-neighbor bond lengths remain closer to the values in unstrained bulk alloys. This implies that in semiconductor alloys tetragonal strain accommodation is mainly obtained through bond-angle distortions, in analogy to the situation in bulk pseudobinary alloys. A model which combines macroscopic elastic theory and the known local structure in bulk pseudobinary alloys is presented, and is found to fit the data very well. [S0163-1829(97)09328-4]

I. INTRODUCTION

The atomic level structure in pseudobinary semiconductor alloys of the type AB_xC_{1-x} (or $A_xB_{1-x}C$) has been extensively studied and is now well understood.[1–4] However, little is still known about the local atomic structure in strained thin films of pseudobinary semiconductors. A strained epilayer may be grown on a substrate having a different lattice constant, provided its thickness is kept below a certain critical value. In this case, the strain due to the lattice mismatch is elastically accommodated by a tetragonal distortion of the grown layer (pseudomorphic growth).

Local atomic investigations on strained semiconductor thin films are mainly limited to first-shell structural information, and report both strained and unstrained bond lengths.[5–19] This paper reports a x-ray-absorption fine-structure (XAFS) investigation of the first three coordination shells around As in $(InAs_xP_{1-x}/InP)_N$ strained-layer superlattices and in unstrained bulk samples of similar composition for a wide As concentration range.

The motivation to extend the comparison to higher coordination shells arises from the yet unanswered question as to how the distortion of the unit cell in the strained layer influences the local atomic structure. In fact, it is now well established that strain due to alloying in bulk pseudobinary alloys is released mainly through bond-angle distortions, as bond lengths (first shell interatomic distances) remain closer to the natural "unstrained" values than to the value predicted by the virtual crystal approximation;[1] the tetrahedral building block is therefore distorted in order to accommodate simultaneously a bimodal distribution of bond lengths and long-range order. In epitaxial semiconductor superlattices, two additional factors may contribute to distort the elementary building block: interface strain and tetragonal distortion. The former is associated with the presence, at the interface between two adjacent layers, of chemical bonds which are absent in either layer. The latter is due to epitaxy with the substrate, and, when growth is pseudomorphic, is a function of lattice misfit and therefore of composition. Differences in the local structure between the thin $InAs_xP_{1-x}$ strained layers in the superlattices and the bulk alloys are expected to arise only from tetragonal strain due to epitaxy with the substrate, as interface strain is absent in this system.

Besides the fundamental interest in determining the strain accommodation mechanisms in these materials, a strong motivation to obtain a local atomic description of the strained-layer structure arises from semiconductor technology. III–V heterostructures are employed in many technological domains requiring remarkable electro-optical characteristics, mainly due to the optical nonlinearities of quantum structures. The presence of strain reduces the symmetry of the crystal, and modifies the band lineups of the charge carriers, adding a further degree of freedom in the design of semiconductor devices based on intentionally strained heterostructures. However, in some cases, nonintentional strain appearing at the interfaces may negatively influence the

performance of the processed devices.

From an applicative point of view, the structural characterization of $InAs_xP_{1-x}/InP$ interface layers in $(InAs_xP_{1-x}/InP)_N$ superlattices is of particular interest in the context of optimization of $InP/In_{0.53}Ga_{0.47}As$ multiple quantum-well heterostructures.[20] In fact, one of the limiting factors of the quality of epitaxially grown heterostructures is a nonintentional compositional interface grading, spread over some monolayers. These undesired layers, consisting, in the $InP/In_{0.53}Ga_{0.47}As$ system, of $InAs_xP_{1-x}$ and $In_{0.53}Ga_{0.47}As_{1-y}P_y$ at the first and second interfaces, respectively, can be studied by depositing *ad hoc* multistructures.[21–25] In this study we investigate *ad hoc* grown $InAs_xP_{1-x}/InP$ layers, allowing the characterization of the first interface, which is the most critical as reported by the majority of authors, as the efficiency of incorporation of As atoms in the just grown InP layers is much greater than that of P in $In_yGa_{1-y}As$.

Although much research has been devoted to an understanding of the electronic consequences of strained-layer growth (see, for example, Refs. 20 and 26–28), very few theoretical studies devoted to understanding the geometric aspects of this problem are found in the literature.[29] An issue that has become of particular importance lately is whether or not macroscopic elasticity theory describes the tetragonal distortions in thin films.[5–9] We have formulated a model, based on macroscopic elasticity theory, which fits our data very well. The model, which will be described in detail, predicts in the $x=1$ limit, a 0.02-Å contraction of the nearest-neighbor bond. This quantity being an upper limit, the effect on the first shell due to tetragonal distortion in the $InAs_xP_{1-x}$ thin layers is indeed at the limit of detectability by XAFS. Therefore it becomes essential to extend the investigation to higher coordination shells, and to extract in a reliable way the important structural parameters. This is possible provided high quality spectra are recorded and a complete multiple-scattering (MS) approach is used in the analysis.

To record high-quality spectra in such extremely As-dilute samples, a high photon flux as well as an adequate fluorescence detection system, which efficiently separates the As fluorescence from the strong elastically scattered background arising from the thick substrate, is needed. Measurements were performed at the Grenoble Italian beamline for Diffraction and Absorption (GILDA) Collaborating Research Group (CRG) beamline[30,31] at the European Synchrotron Radiation Facility (ESRF) (Grenoble, France) providing such state-of-the-art conditions. Moreover, a full MS analysis of the XAFS spectra was performed to obtain a reliable structural picture beyond the first shell on these strained semiconductor superlattices. The present results significantly expand and complete our previously published investigation,[10] which was performed on fewer samples and was limited to the first coordination shell. The results discussed in this paper have been previously presented in a preliminary format.[32]

II. EXPERIMENT

The superlattices consist of 50–1000 periods of thin $InAs_xP_{1-x}$ films (≈ 10 Å), separated by thicker InP layers (≈ 50 Å) epitaxially grown on InP(001) by low-pressure metal-organic chemical vapor deposition (LP-MOCVD), with different As contents. All samples have been thoroughly characterized with more conventional techniques such as high-resolution x-ray diffraction (HRXRD), high-resolution transmission electron microscopy (HRTEM), 4-K Fourier-transform photoluminescence, and As K-edge standing waves and relative simulations.[24,33]

As a result of all these investigations, we were able to obtain a clear picture of the crystalline quality of the superlattices: some were found to be close to perfect, while others had less abrupt interfaces and lower period reproducibility. The superlattice period Δ and the mean As composition $\langle x \rangle$ (averaged over all the superlattice period) were obtained from the HRXRD patterns, by measuring the superlattice peak spacing ($\delta\theta$) and the separation of the zeroth-order superlattice peak from the substrate peak ($\Delta\theta$). Based on the assumption that the As atoms are uniformly distributed in a layer of thickness t and that the interfaces are abrupt, we simulated the experimental rocking curve patterns on the basis of x-ray dynamical diffraction theory, using t as a fitting parameter, and estimated the As content in the ternary layers x from the following formula: $xt=\langle x \rangle \Delta$. The perpendicular mismatch between ternary layer and substrate, $\varepsilon_\perp = (a_\perp - a_{InP})/a_{InP}$, was obtained from the $\Delta\theta$ value, by assuming (a) cubic InP unit cells, (b) pseudomorphic growth of the ternary $InAs_xP_{1-x}$ layers ($a_\parallel = a_{InP}$), and (c) a tetragonal distortion of the ternary layer unit cells following the macroscopic theory of elasticity, $(a_\perp - a_{cubic}) = -2(c_{12}/c_{11})(a_\parallel - a_{cubic})$, where c_{ij} and a_{cubic} are the concentration weighted elastic constants of the alloy and the lattice parameter of bulk $InAs_xP_{1-x}$, respectively. For a discussion of the validity of this method, refer to Ref. 20.

Six bulk $InAs_xP_{1-x}$ samples were prepared as standards for comparison: three polycrystalline samples grown on an Al substrate, and three unstrained bulk samples epitaxially grown on InP(001), with a thickness considerably greater than the critical thickness. The composition of these samples was estimated using 4-K photoluminescence and HRXRD for the former and the latter respectively.

In Tables I(a) and I(b), we report the composition and thicknesses of the six bulk samples (B_1–B_6) and characterization data relative to the seven superlattice samples (H_1–H_7), including As content in the ternary layers, x, superlattice period Δ, best-fit ternary layer thickness t, number of periods N, and perpendicular mismatch between ternary layer and substrate, $\varepsilon_\perp$.

XAFS measurements at the As K edge were performed at the GILDA beamline at the ESRF.[30] The monochromator operated with Si(311) crystals in a dynamical sagittal focusing mode.[31] The energy resolution and flux were approximately 1.2 eV and $\approx 5\times 10^9$ photons/s on the sample, with a focal image of about 1 mm^2. Harmonic rejection was performed by detuning the two crystals. The XAFS measurements were performed in the transmission mode on the bulk samples grown on Al, and in the fluorescence mode on all the others, using a hyperpure Ge detector with a high-energy resolution (≈ 300 eV at 11 keV) to discriminate the As $K\alpha$ fluorescence yield (at energy $E\approx 10.5$ keV) from the elastically scattered background [$10.7 \leq E(\text{keV}) \leq 12.7$]. In fact a major problem in using fluorescence detection with these

TABLE I. (a) Characteristics of bulk $InAs_xP_{1-x}$ samples: substrate (column 2), As content x (column 3) and thickness t (μm) (column 4). (b) $(InAs_xP_{1-x}/InP)_N$ superlattice characterization data: growth code (column 2), As content in the ternary layers x (column 3), superlattice period Δ (Å) (column 4), best-fit ternary layer thickness t (Å) (column 5), number of periods N (column 6), and perpendicular mismatch between ternary layer and substrate $\varepsilon_\perp$ (column 7).

(a)

Sample	Substrate	x	t (μm)
B_1	Al	1.00	20
B_2	Al	>0.65	20
B_3	Al	0.56	30
B_4	InP	0.50	0.2
B_5	InP	0.41	0.2
B_6	InP	0.21	0.2

(b)

Sample	Code	x	Δ (Å)	t (Å)	N	$\varepsilon_\perp$(%)
H_1	141	0.59	91	10	50	4.0
H_2	137	0.33	90	10	50	2.3
H_3	183	0.24	63	13	360	1.6
H_4	157	0.20	93	15	50	1.4
H_5	182	0.19	53	18	300	1.3
H_6	114	0.17	60	10	1000	1.2
H_7	032	0.05	77	10	100	0.3

samples arises from the excitation of Bragg reflections from the substrate or from the superlattice, the direction of which may fall into the solid angle of acceptance of the detector at some energy during the scan, introducing deformations on the XAFS spectrum. The detector was positioned on the horizontal plane, at 90° with respect to the direction of the incoming beam. The portion of solid angle accepted by the detector was $\Delta\Omega/4\pi \approx 2.5\times10^{-3}$. Total count rates ranged from 3×10^2 to 1.8×10^4 photons/s, depending on the total As content in the sample, with a negligible loss in detector response linearity. The polarization vector of the beam was directed along the (011) crystallographic direction. Measurements were performed at $T=77$ K in order to reduce thermal damping of the signal and extend the useful range for the analysis, except for sample H_2, measured only at room temperature. Sample B_1 (pure InAs) was measured at both temperatures. Transmission spectra were recorded in the energy range 11.7–13.5 keV ($k_{max}=20.7$ Å^{-1}), while fluorescence spectra were recorded up to approximately 12.7 keV ($k_{max} \approx 14$ Å^{-1}) due to the lower signal-to-noise ratio.

A qualitative preliminary data analysis was performed using standard XAFS data analysis programs. The pre-edge and the atomic absorption background were simulated with a linear function and a cubic spline respectively. The XAFS signals were normalized using the function $J\times[1-8/3(E-E_0)/E_0]$, where J and E_0 are the discontinuity of the absorption spectrum and the energy corresponding to the maximum derivative at the absorption edge, respectively. Figure 1 illustrates normalized $k\chi(k)$ signals and amplitudes of the Fourier transforms (FT's) of the $k^2\chi(k)$ signals for the transmission spectra [Figs. 1(a) and 1(b)] and for the fluorescence spectra [Figs. 1(c) and 1(d)]. FT's were performed using a Hanning window in the k range 3.0–20.0 and 3.0–10.0 Å^{-1} for the transmission and fluorescence spectra, respectively. Contributions arising from at least three coordination shells around As are clearly visible in all the FT's. The main features can be attributed to single scattering paths, but MS paths also contribute as will be illustrated in Sec. III, especially in the region between the second and third shells. The first peak arises from the As-In first-shell interaction. The shoulder (or small peak) appearing on the low-R side of this first peak is due to the shape of the In backscattering amplitude, and is typical of heavy backscatterers. The second peak is mainly due to As-P and As-As second-shell interactions; its intensity and shape are therefore strongly dependent on sample composition. Finally, the third peak arises from third-shell In atoms, interacting with the central As atom through second-shell P or As atoms. Due to residual Bragg peaks in the central part of the spectrum relative to sample H_4, the analysis relative to this sample was limited to first shell information, and its FT is not shown.

III. DATA ANALYSIS

Quantitative data analysis was performed using the GNXAS software package.[34] These programs perform an *ab initio* analysis based on MS calculations and on a rigorous fitting procedure directly on the raw experimental data. Signals associated with atomic arrangements related to two- and three-body distribution functions are calculated using fast algorithms based on the evaluation of continued fractions.[35] The general theory of configurational damping of the signal associated with a given n-body configuration is used to take into account peak broadening.[36] Atomic phase shifts are calculated in the muffin-tin approximation, based on self-consistent relativistic calculations and the effect of inelastic losses is included through a complex Hedin-Lundqvist potential. The muffin-tin radius was set equal to 0.75 the Nor-

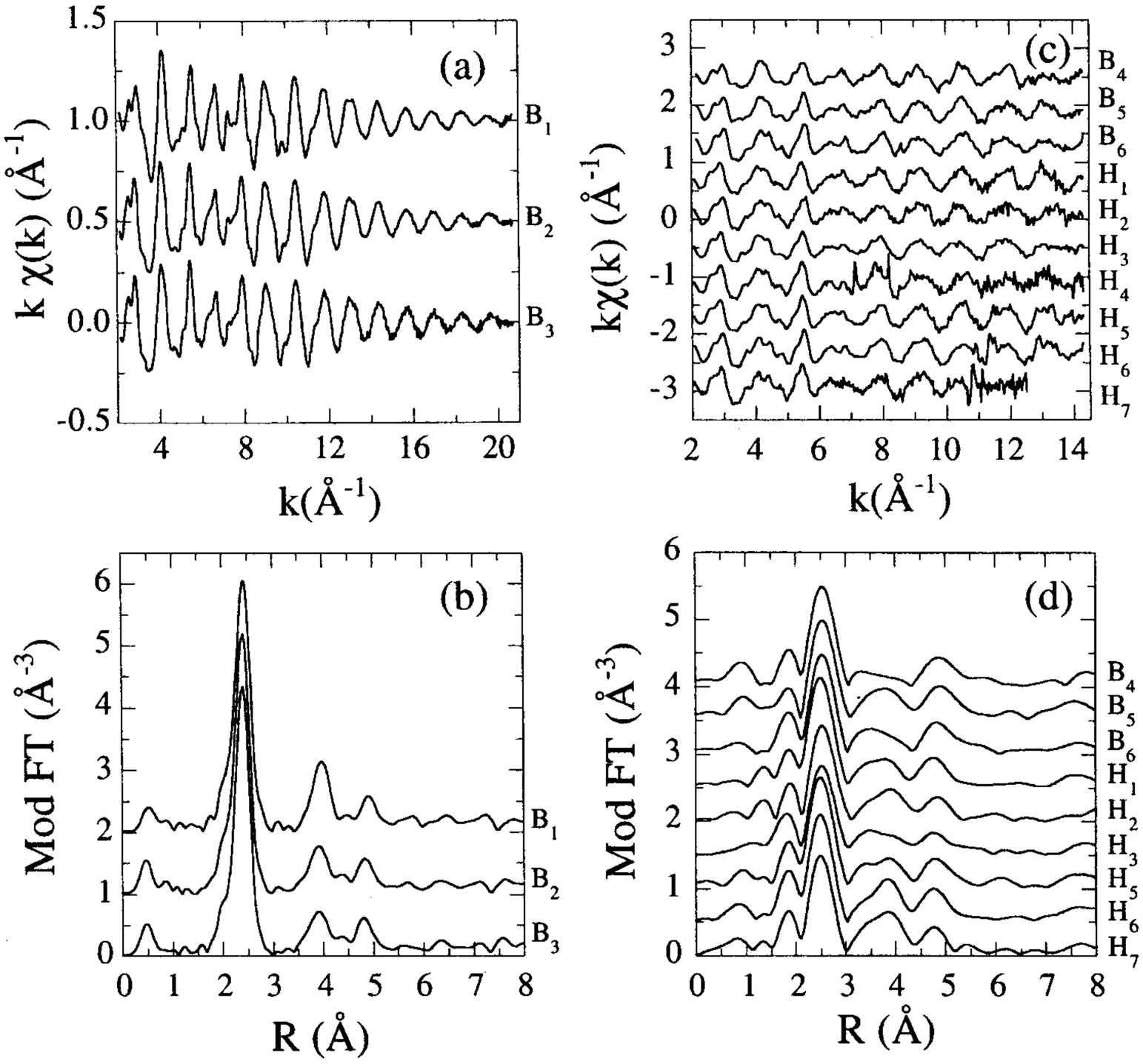

FIG. 1. (a) Normalized $k\chi(k)$ signals and (b) amplitudes of the Fourier transforms of the $k^2\chi(k)$ signals for the transmission spectra. FT's have been performed in the k range 3.0–20.0 Å^{-1}. (c) Normalized $k\chi(k)$ signals and (d) amplitudes of the Fourier transforms of the $k^2\chi(k)$ signals for the fluorescence spectra. FT's have been performed in the k range 3.0–10.0 Å^{-1}.

man radius. The calculated phase shifts were found to be insensitive to small variations of this parameter.

As a preliminary check of the reliability of the data analysis procedure based on the GNXAS package we analyzed the first shell signal of all the samples with traditional Fourier filtering techniques using experimental amplitudes and phases from sample B_1; we found the first shell parameters to be equal, within the errors, to those found by the *ab initio* method, thus indicating that the latter does not introduce systematic errors. This check is possible only for the first shell, since the presence of significant MS contributions precludes the use of standard analysis for the second and third shells.

Returning now to the GNXAS analysis, the calculated signals included in the model $\chi(k)$ function are all the single-scattering contributions relative to the first three coordination shells around As and the most important MS contributions. The former have already been listed in Sec. II, and trivially correspond to the zinc-blende structure. The latter consist of three triangular paths involving first-shell atoms (the As-In-In, triangle, hereafter called T_1), and second shell atoms (the As-In-P and As-In-As triangles, hereafter called T_2 and T_3, respectively). These paths are illustrated in Fig. 2. The MS signals considered are therefore all relative to triangular paths involving the tetrahedral angle (109.47°), and therefore give rise to relatively small MS amplitudes in the extended XAFS region. However, the inclusion of MS contributions in this system, in particular of that arising from the T_3 triangle, has proved to be essential for a correct determination of the structural parameters relative to the second-shell As-As distance, as will be illustrated below.

Our data analysis procedure consisted in finding the set of

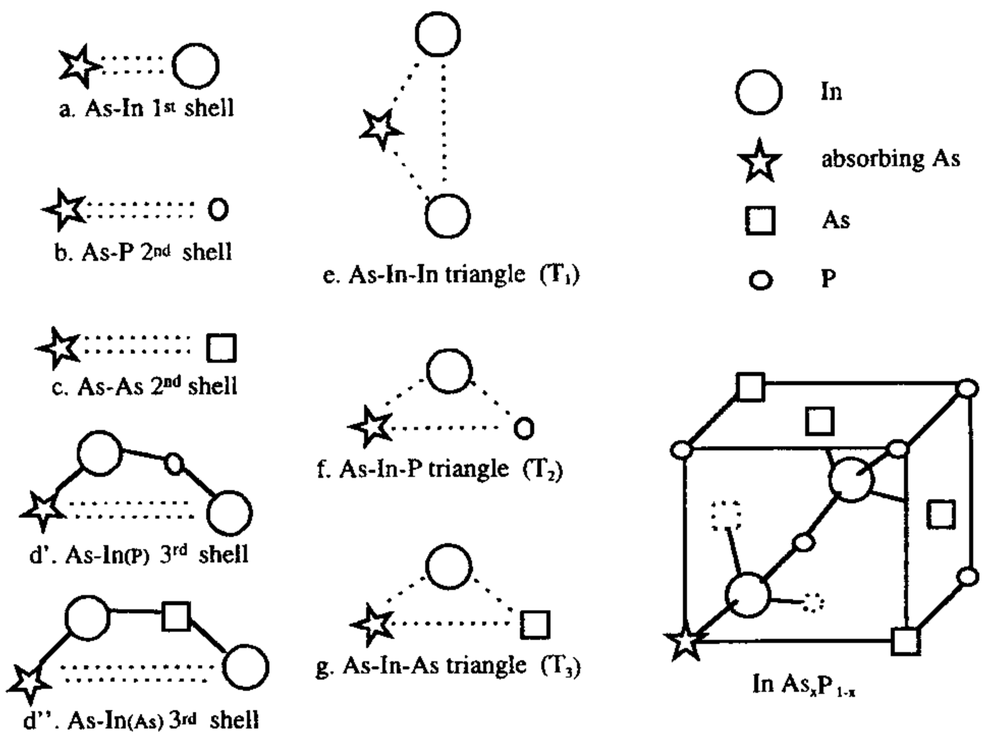

FIG. 2. Atomic configurations relative to all the calculated signals included in the model $k\chi(k)$ function, relative to single [(a), (b), (c), and (d)] and multiple [(e), (f), and (g)] scattering paths from the central As atom in $InAs_xP_{1-x}$. An average signal has been used to account for the two third-shell As-In interactions, relative to a third-shell In atom bonded to second-shell P (d') or As (d'') atoms, respectively.

best-fit structural parameters relative to the first three coordination shells in all samples (except H_4, as explained previously). The model function chosen for the simulation of the different coordination shells was based on the known local structure of bulk pseudobinary semiconductor alloys, which is summarized in Sec. IV. In the fitting procedure, total coordination numbers were assumed equal to nominal values in the zinc-blende structure: $N_{\text{As-In}}=4$, $N_{\text{As-As}}+N_{\text{As-P}}=12$, and $N_{\text{As-In-P-In}}+N_{\text{As-In-As-In}}=12$ for the first, second, and third coordination shells around As, respectively. First-shell fitting parameters were the As-In bond distance $R^{(1)}_{\text{As-In}}$ and the mean-square relative displacement σ_1^2. The second shell was fitted with two different contributions due to As-P and As-As interactions, respectively. The structural parameters relative to these contributions are identical to those of the ''long bonds'' in triangles T_2 and T_3, respectively, and therefore only a limited number of structural parameters was introduced. The fitting parameters were: relative coordination, $N_{\text{As-As}}/N_{\text{As-P}}$; bond angles θ_{T2} and θ_{T3} from which As-P and As-As distances $R^{(2)}_{\text{As-P}}$ and $R^{(2)}_{\text{As-As}}$ were calculated, respectively. Due to strong correlation of second shell amplitude parameters, only one average mean square relative bond angle displacement, $\sigma^2_{\theta_{T2}}=\sigma^2_{\theta_{T3}}=\sigma^2_\theta$ was used in the model. This parameter proved to be affected by a large error indicating the low sensitivity of the minimizing procedure to variations of σ^2_θ. In the fittings relative to the fluorescence recorded spectra, due to the lower signal-to-noise ratio, in all cases where the second-shell signal was found to contain both As-As and As-P contributions (samples B_4, B_5, B_6, H_1, H_2, H_3, and H_5) reliable second-shell coordination numbers could not be obtained unless σ^2_θ was fixed.

As for the third shell, two different As-In distances are expected to coexist in the alloys, relative to In atoms interacting with the central As through P and As second-shell atoms respectively. In order to limit the number of fitting parameters, the third shell was fitted with one average As-In contribution, instead of using two contributions for the two different third-shell distances expected. The fitting parameters were the As-In average bond distance $\langle R^{(3)}_{\text{As-In}}\rangle$ and the average mean-square relative displacement σ_3^2. The presence of two separate distances was confirmed by the larger value of σ_3^2 found in the alloys with respect to the value found in binary InAs. Due to strong correlation between the values of $R^{(3)}_{\text{As-In}}$ and σ_3^2, the latter parameter was fixed to the value which best reproduced the amplitude of the third peak in the Fourier transform.

Due to the low sensitivity of the minimization procedure to variations in parameters involved in the $\chi(k)$ signal only through MS paths, such as $R^{(1)}_{\text{In-P}}$ and θ_{T1}, these were fixed to their nominal values in the binary compounds, i.e., 2.54 Å and 109.47°, respectively. The parameters S_0^2 and E_0 were fixed to values obtained from the best fit of the spectrum relative to pure InAs (sample B_1). These were found to be $S_0^2=0.79\pm0.07$ and $\Delta E_0=(6.0\pm0.6)$ eV, respectively.

The effect of the linear polarization of the beam on the measured coordination numbers for the superlattice samples was estimated by weighting each scattering path (single and multiple scattering) with a coefficient calculated in the plane wave approximation,[37] and assuming an undistorted geometry. The normalized polarization dependent coefficient for each $(\mathbf{R}_1,\mathbf{R}_2,\ldots,\mathbf{R}_n)$ path in this case given by the relation

$$\frac{3(\hat{\varepsilon}\cdot\mathbf{R}_1)(\hat{\varepsilon}\cdot\mathbf{R}_n)}{\mathbf{R}_1\cdot\mathbf{R}_n}, \tag{1}$$

where $\hat{\varepsilon}$ is the polarization unit vector of the incident beam. The validity of this method has been successfully tested on a standard monocrystal of hcp Co, by simulating the signals relative to spectra recorded in normal incidence and grazing incidence.[38] Corrections to measured total coordination numbers due to beam polarization effects were found to be negligible. This confirms our assumption on total coordination numbers being equal to those in the zinc-blende structure.

The maximum number of minimized parameters was equal to 8, whereas the estimated ''number of independent points,'' a number appropriate for discussing the reliability of Fourier filtering analysis and calculated using the formula $(2/\pi)\Delta k\Delta R$,[39] exceeded 30. However, the fits were performed directly on the raw data, with no Fourier-filtering procedures, so that the real number of independent points exceeded 170. An example of the quality of the fit is shown in Fig. 3, where we compare the raw experimental $k^2\chi(k)$ relative to sample B_2 to its best-fit model function. The fit is performed directly on the raw data up to a $k_{\max}\approx20.7$ Å^{-1}, using k^3 weight. The main residual in the low-k region is due to coordination shells beyond the third which have not been included in the model, but which are clearly present in the XAFS signal, as confirmed by the Fourier transform shown in Fig. 4. In Fig. 4(a) we compare the amplitude of the FT's of the $k^2\chi(k)$ experimental function with the corresponding best-fit model function. The contributions arising from the first three coordination shells around As are clearly visible, and are fairly well reproduced by the model. For all samples, the first peak was found to be well reproduced by the contribution of four In atoms. As for the second peak, all samples have been tested for the presence of As-As and As-P second-shell interactions. In some superlattice samples with low As content, however, the best fits were obtained when the ratio $N_{\text{As-As}}/N_{\text{As-P}}$ was set equal to zero,

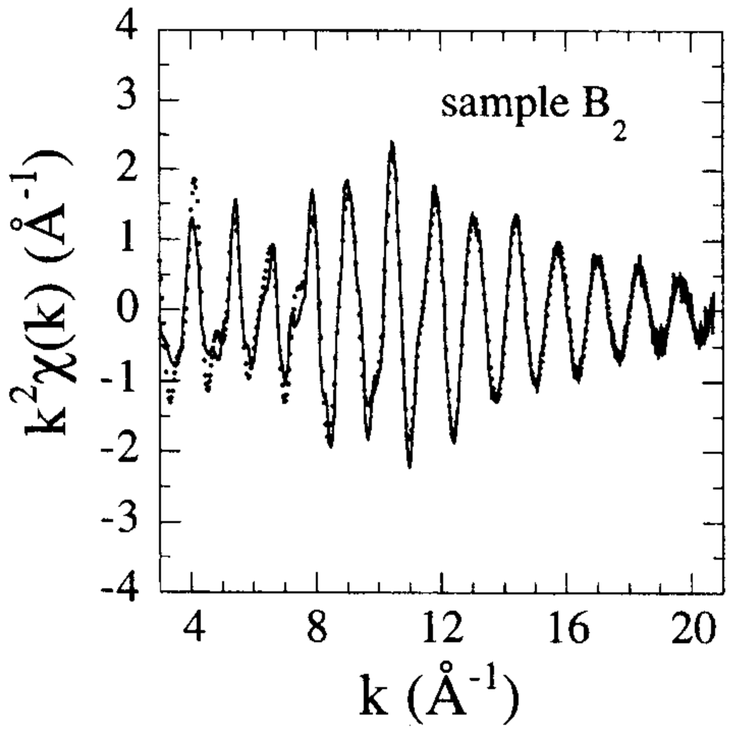

FIG. 3. Raw experimental $k^2\chi(k)$ relative to sample B_2 (solid line) and its best-fit model function (dotted line). The fit is performed directly on the raw data up to a $k_{\max}\approx20.7$ Å^{-1}, using a k^6 weight. The residual in the low-k region is due to coordination shells beyond the third, which have not been included in the model.

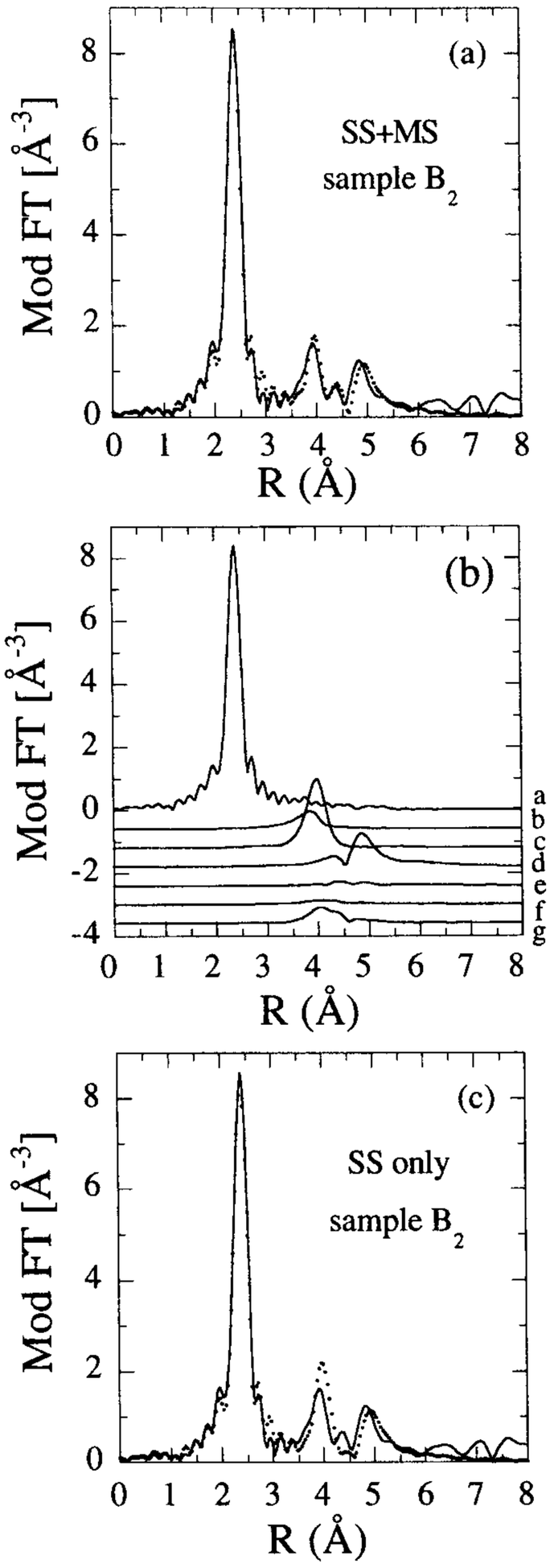

FIG. 4. (a) Amplitudes of the Fourier transforms of experimental $k^2\chi(k)$ for sample B_2 (solid line) and of its best-fit model function (dotted line). FT's have been performed in the k range 3.0–20.0 Å^{-1}. (b) Fourier transforms of the $k^2\chi(k)$ calculated signals relative to all the scattering paths included in the model function shown in 4(a): the associated atomic configurations are shown in Fig. 2. (c) As in (a), but the fit is performed with a model function which does not include MS contributions.

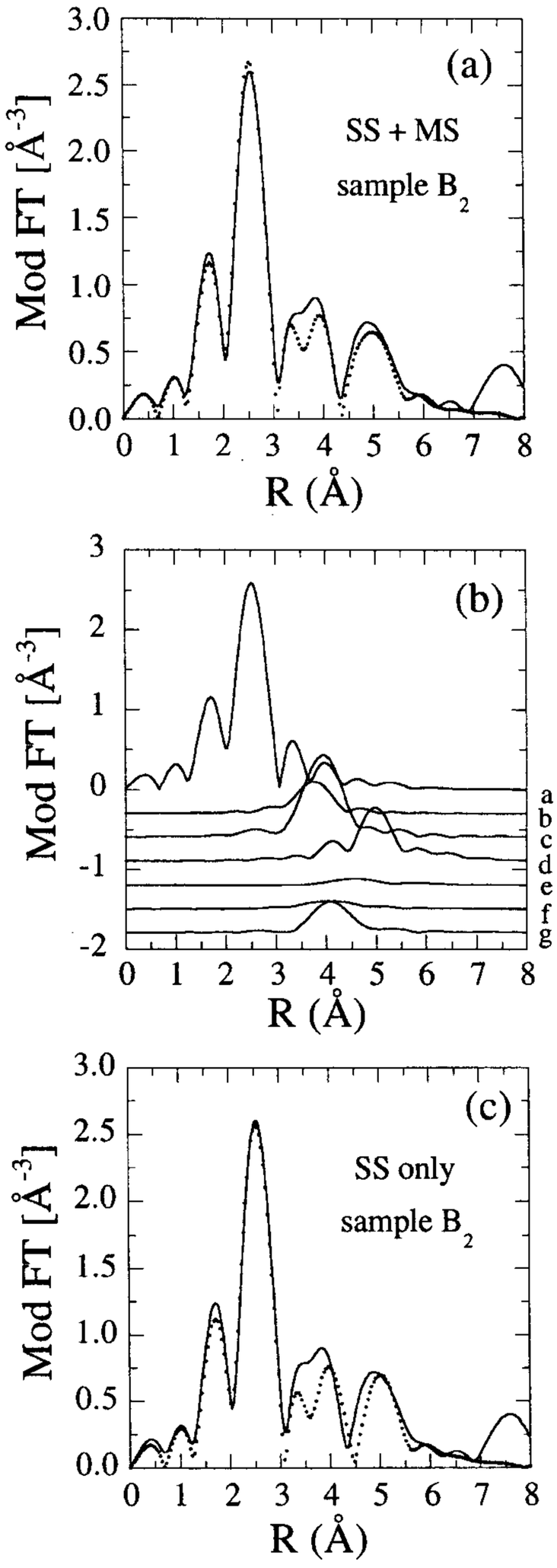

FIG. 5. As in Fig. 4, but for a fit performed up to $k_{max} \approx 10$ Å^{-1}, using a k_3 weight. FT's have been performed in the k range 3.0–10.0 Å^{-1}.

i.e., no contribution due to As-As interactions was detected. Finally, the third peak was reproduced by an average signal due to 12 In atoms bonded to the second-shell As (or P) atoms.

To illustrate the importance of the MS terms in this system, Fig. 4(b) shows the calculated signals relative to the best fit of sample B_2 due to the various paths included in the model function. Note that the MS terms, and in particular signal g (triangle T_3), are important in the R range lying between the second and third shells. Figure 4(c) shows the quality of the fitting when the model does not contain MS terms. By comparing Fig. 4(a) with Fig. 4(c), we deduce that MS terms improve the quality of the fitting, in particular in the R-space region between the second and third peaks. A correct reproduction of the position and amplitude of the second peak, as well as of the small peak lying between the second and third peaks is possible only when MS terms are considered, allowing one to obtain a more reliable set of parameters for the second and third shells. In fact, the absence of MS terms in the model function leads to an overestimation of $R^{(2)}_{\text{As-As}}$ of up to 0.1 Å, a result which is not physically explainable.

Due to spurious signals on the spectra of the most diluted samples, caused by small Bragg peaks not efficiently filtered by the detection system, some of the fittings had to be limited to a maximum energy of 12 250 eV (corresponding to a

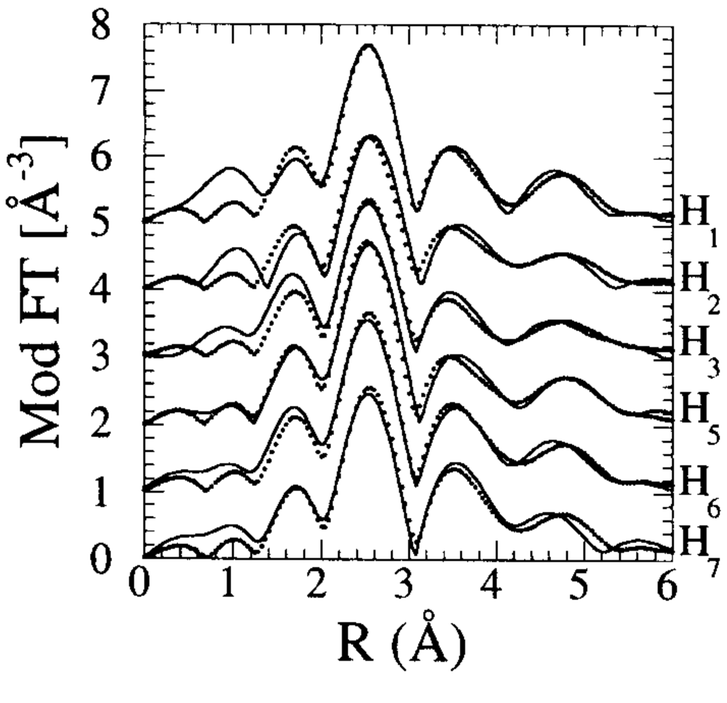

FIG. 6. Amplitudes of the Fourier transforms of experimental and fitted $k^2\chi(k)$ functions for all superlattice samples. The FT has been performed in the k range 3.0–10.0 Å^{-1}.

$k_{max}\approx 10$ Å^{-1}). In order to minimize systematic errors due to the different analysis, the final fittings on all samples were performed in the same restricted k range, using a k^3 weight. In Figs. 5(a)–5(c), we show the analog of Figs. 4(a)–4(c) relative to the restricted k range fittings. This fitting enhanced the relative amplitude of the higher shells and of the MS terms with respect to that of the first shell.

The "visual" improvement of the fits resulting from the addition of the MS terms, which is evident in Figs. 4 and 5, is also statistically significant, as can be understood from the following argument. The minimized function is proportional to a chi-square variable χ^2_ν, where the degrees of freedom ν are $\nu=N-p$, with N the total number of points in the spectrum and p the number of fitted parameters. Due to the presence of high-frequency residuals deriving from coordination shells higher than the third, which we have not included in the model function, we cannot compare the value of χ^2_ν at minimum with standard tables. However, we may use the properties of χ^2_ν to compare fits performed with and without MS contributions using the fact that the number of fitting parameters p is the same in the two cases. The standard deviation of χ^2_ν is

$$\Delta\chi^2_{\text{stat}}=\sigma_{\chi^2}=\sqrt{2\nu}. \tag{2}$$

We define $\Delta\chi^2$ as the increase of χ^2_ν induced by the absence of MS terms:

$$\Delta\chi^2=\chi^2_{\text{No MS}}-\chi^2_{\text{MS}} \tag{3}$$

where $\chi^2_{\text{No MS}}$ and χ^2_{MS} are the χ^2_ν values at the minimum for the fits performed without and with the MS terms, respectively. We found that $\Delta\chi^2$ is significantly larger than $\Delta\chi^2_{\text{stat}}$; for the examples in Figs. 4 and 5, $\Delta\chi^2\approx 10\,\Delta\chi^2_{\text{stat}}$, and $\Delta\chi^2\approx 70\,\Delta\chi^2_{\text{stat}}$, respectively.

The fits relative to all the superlattice samples are illustrated in Fig. 6, where the amplitude of the FTs of the experimental and model $k^2\chi(k)$ functions are compared. The best-fit values of interatomic distances for the bulk and strained-layer samples are plotted in Figs. 7 and 8, respectively, while second-shell As-As coordination and mean-square relative displacement values are summarized in Table II.

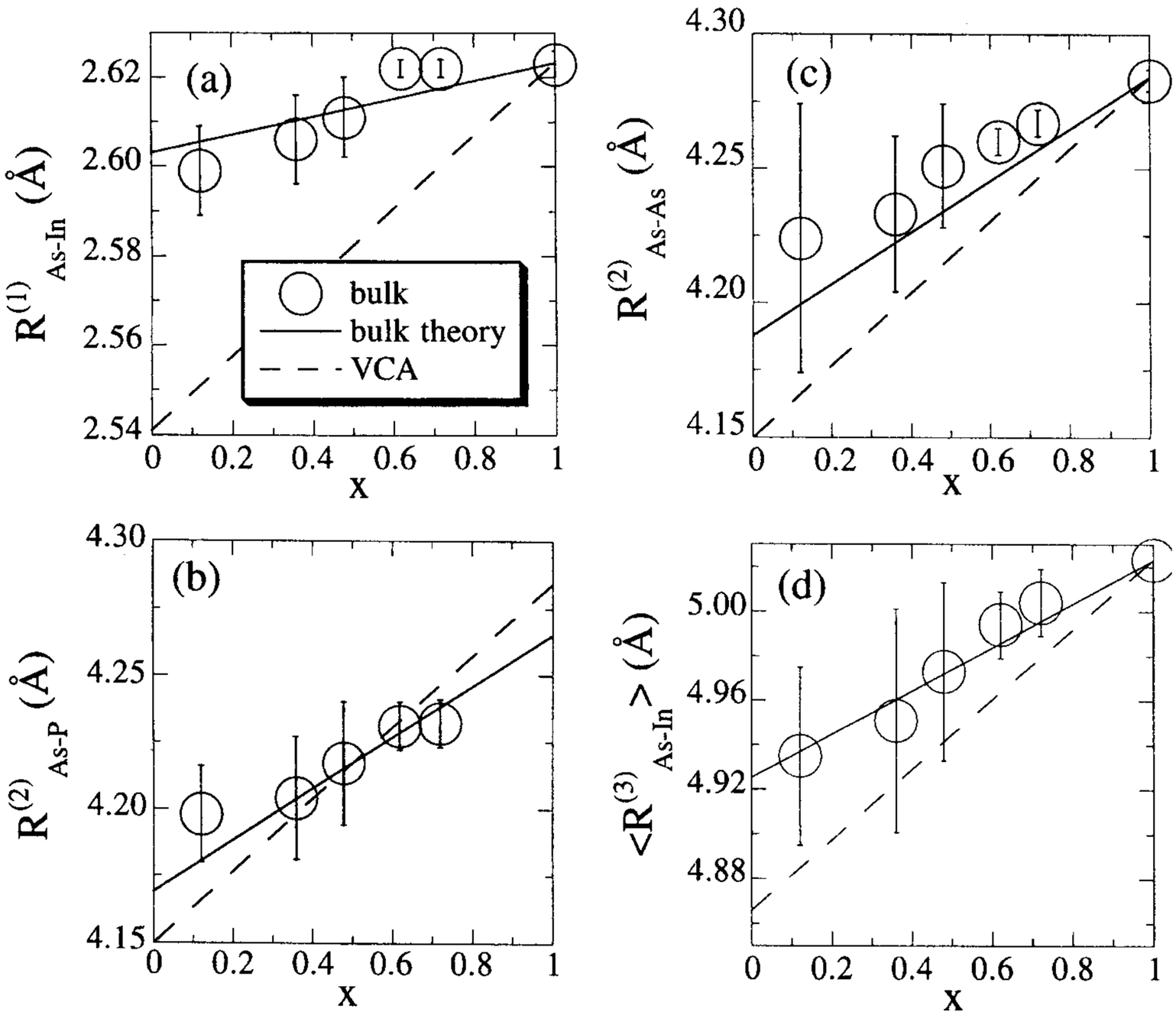

FIG. 7. Comparison between best-fit values of interatomic distances for the bulk samples (circles), theoretical prediction valid for bulk alloys from Ref. 4 (solid line), and the virtual crystal approximation (dashed line): (a) first-shell As-In; (b) second-shell As-P; (c) second-shell As-As; (d) average third-shell As-In.

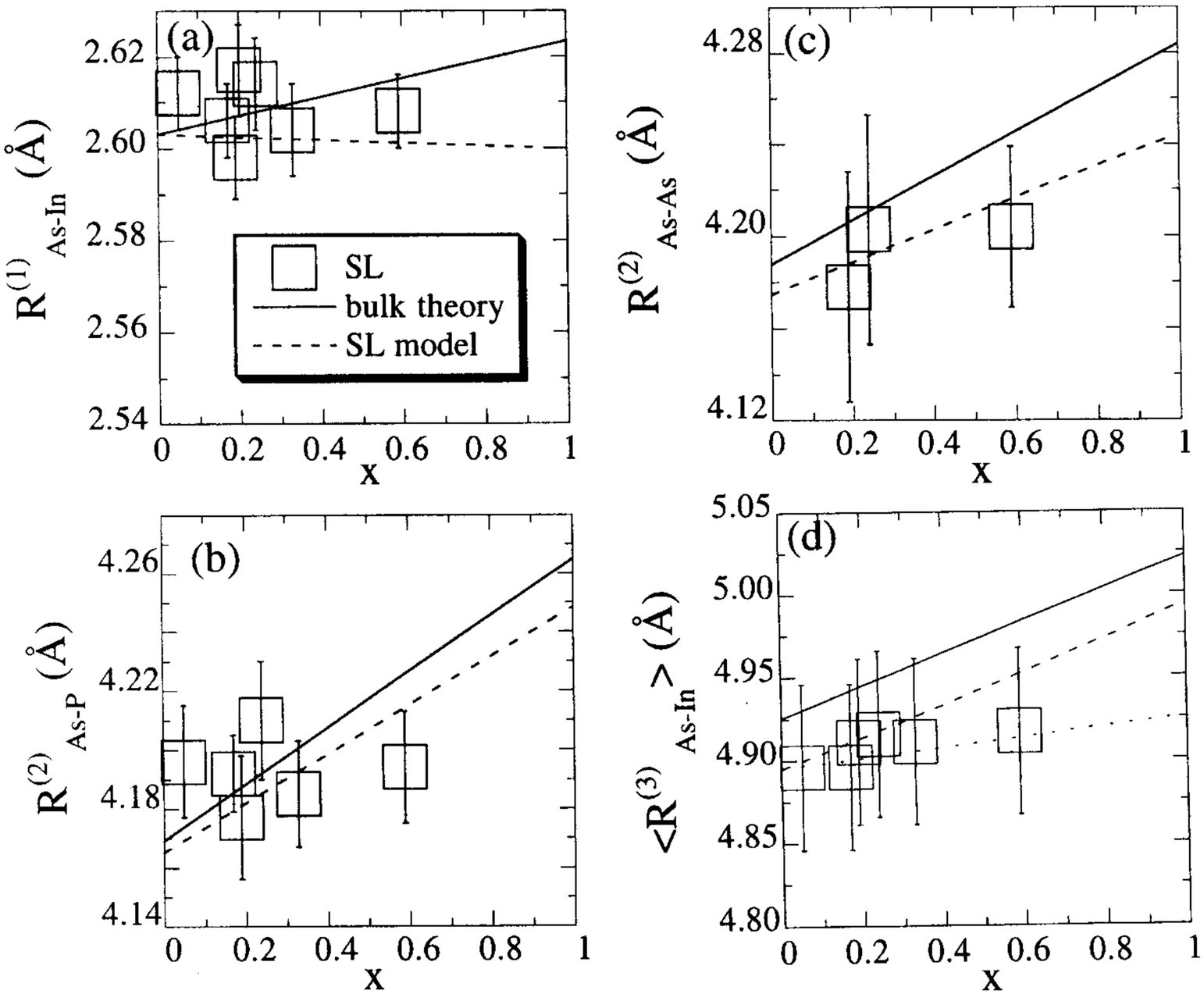

FIG. 8. Comparison between best-fit values of interatomic distances for the superlattices (squares), theoretical prediction valid for bulk alloys from Ref. 4 (solid line), and the theoretical prediction of the strained layer model described in the text (dashed line): (a) first-shell As-In; (b) second-shell As-P; (c) second-shell As-As; (d) third-shell As-In. The measured values of $R^3_{\text{As-In}}$ are compared in (d) to two differently weighted averages of $R^{(3)}_{\text{As-In}_P}$ and $R^{(3)}_{\text{As-In}_{As}}$: assuming a random distribution of As and P atoms on the mixed lattice (dashed line), and based on measured second-shell coordination numbers (dotted line).

IV. DISCUSSION: BULK ALLOYS

In the following we shall give a brief overview of the local structure in bulk AB_xC_{1-x} pseudobinary alloys. We shall then discuss our experimental results on the bulk $InAs_xP_{1-x}$ alloy samples in the framework of this picture.

The pioneering work of Mikkelsen and Boyce[1] was the first to shed light on the local atomic structure in bulk pseudobinary semiconductor alloys. Nearest-neighbor bond-length values (R_{AB} and R_{AC}) were found to be much closer to those in the binary compounds than to those expected if the atoms were positioned in their average ''crystallographic'' positions. The observation of ''rigid'' bonds and therefore of a bimodal bond length distribution ($R_{AB} \neq R_{AC}$) in semiconductor alloys was, at the time, in contrast with the existing assumption on the local structure in these materials, based on the virtual-crystal approximation (VCA), where all atoms were assumed to lie on an undistorted ''virtual'' lattice with a concentration averaged lattice constant [$R_{AB}=R_{AC}=R$, where $R=(\sqrt{3/4})\langle a\rangle$]. This finding led to the formulation of several model structures for bulk pseudobinary alloys[2,40,41] in the attempt to reconcile the short-range order features observed with XAFS with the coexisting long-range order seen with conventional diffraction techniques, where these alloys were found to closely follow Vegard's law. These models are based on a relatively distorted chemically ordered (A) sublattice, whereas the chemically disordered (B and C) sublattice remains substantially closer to the VCA prediction.

On a local scale, this picture is consistent with distorted tetrahedra, where bond angles adapt to allow the central A atom to move closer to the C (or B) atoms and further away from the B (or C) atoms. Bond-angle ''floppiness'' has been observed in a number of semiconductor alloys, and can be intuitively understood, since bond bending force constants are much weaker than bond stretching ones.[42] This behavior has been explained successfully by using rigid-ion force-constant potentials like the Kirkwood and Keating models, to describe the atomic relaxations.[3,43,44]

Recently, an analytic solution has been formulated,[4] al-

TABLE II. Second-shell As-As coordination $N_{\text{As-As}}$ (column 2), first-shell As-In mean-square relative displacement σ_1^2 (column 3), bond angle mean-square fluctuation σ_θ^2 (column 4), and average third-shell As-In mean-square relative displacement σ_3^2 (column 5). Values in brackets are relative to room-temperature measurements. When the error is not indicated, the parameter has been kept constant in the fit, as described in the text.

Sample	$N_{\text{As-As}}$	σ_1^2 (10^{-3} Å^2)	σ_1^2 (deg^2)	σ_3^2 (10^{-3} Å^2)
B_1	12	1.8± 0.2	4±1	10±2
		(3.8± 0.4)		
B_2	8±1	2.4± 0.2	5±1	13
B_3	7±1	2.4± 0.3	4±1	13
B_4	6±2	4 ± 1	4	12
B_5	5±2	3 ± 1	4	13
B_6	1±2	4 ± 1	4	12
H_1	2±2	2 ± 1	4	15
H_2	(1±2)	(4 ±2)	(4)	(20)
H_3	2±2	4 ± 4	4	22
H_4		3 ± 2		
H_5	2±2	2 ± 2	4	16
H_6	0	2 ± 1	5±4	16
H_7	0	2 ± 1	5±4	20

lowing one to calculate mean bond lengths for the nearest- and next-nearest-neighbor distances in quaternary zinc-blende alloys of the type $A_{1-x}B_xC_{1-y}D_y$. In the framework of this theory, pseudobinary and binary alloys are treated as the special cases $x=0$ and $x=y$ (with $A=C$ and $B=D$), respectively. First- and second-shell interatomic distances measured on a number of alloy systems[1,2,16,45] are found to follow this prediction closely.

In Figs. 7(a)–7(c), we compare our experimental results relative to the bulk samples (circles) to the above-mentioned theoretical prediction for the first- and second-shell interatomic distances (solid line). The VCA prediction is also shown (dashed line).

The first shell around As was found to be well reproduced by the contribution of four In atoms at a distance $R^{(1)}_{\text{As-In}}$ which decreases very slightly as $x\rightarrow 0$, remaining much closer to the value in pure InAs than to the VCA prediction, as can be seen in Fig. 7(a). The agreement with the above-mentioned theory is very good, confirming that the $InAs_xP_{1-x}$ alloy follows the general behavior of pseudobinary semiconductor alloys.

The second shell in bulk $InAs_xP_{1-x}$ alloys is expected to split into two subshells, an As-P shell and an As-As shell, which, however, remain quite close to each other and to the VCA prediction. In Figs. 7(b) and 7(c) our experimental results for the second-shell interatomic distances, $R^{(2)}_{\text{As-P}}$ and $R^{(2)}_{\text{As-As}}$ compare well to the theoretical prediction.

The third shell is also expected to split into two subshells, relative to In atoms bonded to second-shell P and As atoms, respectively. These two subshells lie at distinct distances, $R^{(3)}_{\text{As-In}_\text{P}}$ and $R^{(3)}_{\text{As-In}_\text{As}}$ respectively, as the In sublattice is distorted in order to accommodate the almost constant In-P (and In-As) bond length. To our knowledge, no previous experimental evidence of this third shell splitting exists. Moreover, no theoretical predictions have been made for third-shell bond lengths in these alloys. In the absence of theoretical predictions or experimental results, these were compared to an extrapolation of the above theory [Fig. 7(d)]. The solid line is a concentration weighted average of the two extrapolated third shell As-In distances: $R^{(3)}(x)=(1-x)\ R^{(3)}_{\text{As-In}_\text{P}} + xR^{(3)}_{\text{As-In}_\text{As}}$. The agreement is excellent, providing a proof of the validity of this theory also for third-shell distances.

Best-fit values of the structural parameters which determine the amplitude of the XAFS signal are listed in Table II. First-shell mean-square relative displacement (MSRD) values are close to the value found for pure InAs, while third-shell MSRD values are larger and consistent with the coexistence of two distinct third-shell As-In interatomic distances. In fact, the expected composition independent subshell separation $\Delta R_3=R_3(\text{As-In}_\text{As})-R_3(\text{As-In}_\text{P})$ is approximately 0.06 Å, leading to an increase $\Delta\sigma^2_3(\text{static})\approx 3.5\times 10^{-3}$ Å^2. Second-shell coordination numbers obtained are consistent with a random distribution of As and P atoms on the chemically disordered lattice for all the investigated bulk samples, in agreement with the known complete miscibility of pseudobinary solid solutions.[2,41,45] Bond-angle fluctuations σ_θ are found to be relatively constant and equal to $\approx 2°$ throughout the composition range $0.6\leqslant x\leqslant 1.0$.

V. DISCUSSION: STRAINED LAYERS

Two effects influence the values of the measured structural parameters in strained-layer superlattices, and must be taken into account to make a comparison with bulk samples. The first effect is related to the loss of cubic symmetry of the crystalline structure induced by tetragonal distortion; the second is due to the limited thickness (about 3 ML) of the ternary layers in our samples.

In a tetragonally distorted zinc-blende structure, shell splitting may occur: atoms in the same coordination shell in an undistorted cubic system are found to lie at two slightly different average distances with respect to a central atom. In a strained layer of InAs epitaxially grown on an InP substrate, if pseudomorphic growth is assumed, second-shell As-As distances relative to atoms lying on the growth plane ($R_{2\parallel}$) are expected to be equal to second-shell P-P distances in the substrate, while distances relative to second-shell As atoms lying on planes perpendicular to this plane ($R_{2\perp}$) are a function of tetragonal distortion. The ratio between the number of atoms ''seen'' using XAFS at distance $R_{2\perp}$ and $R_{2\parallel}$, respectively, $N_\perp/N_\parallel$, is a function of beam polarization direction. In a polarization-averaged situation $N_\perp=8$ and $N_\parallel=4$, and $N_\perp/N_\parallel=2$. In our geometry, following Eq. (1), $N_\perp\approx 9$ and $N_\parallel\approx 3$, and $N_\perp/N_\parallel\approx 3$.

A similar argument may be extended to the third shell, even though here the two subshell distances R_3' and R_3'' are both a functions of tetragonal distortion, as third-shell atoms lie in all cases out of the growth plane. In a polarization averaged situation the number of atoms lying at distance R_3'' (further from the growth plane) is $N''=4$, and those at distance R_3' (closer to the growth plane) is $N'=8$, with $N''/N'=0.5$. In our geometry, following Eq. (1), $N''\approx 5.5$ and $N'\approx 6.5$, and $N''/N'\approx 0.85$.

The second effect, related to the limited extension of the $InAs_xP_{1-x}$ layers in the growth direction, changes the relative number of second-shell P and As atoms, and therefore also the relative number of third-shell In_P and In_As, with respect to the situation in a bulk sample of $InAs_xP_{1-x}$. In fact, the thinner the $InAs_xP_{1-x}$ layer embedded in InP, the higher the number of second-shell P atoms with respect to As atoms. In the limiting case of $x=1$ (pure InAs), the ratios $N_\perp(\text{As-P})/N_\perp(\text{As-As})$, $N'(\text{As-In}_\text{P})/N'(\text{As-In}_\text{As})$, $N''(\text{As-In}_\text{P})/N''(\text{As-In}_\text{As})$ increase from zero (in bulk InAs) to $\frac{1}{3}$, $\frac{1}{6}$, and $\frac{1}{3}$, respectively for a 3-ML InAs film embedded in InP. These considerations are used in the following in order to correctly interpret the values of interatomic distances measured for the tetragonally strained layers.

The results relative to the interatomic distances in the superlattices are shown in Figs. 8(a)–8(d) (squares). There is evidence of deviations from the behavior of bulk alloys described above: the interatomic distances in the strained layers are on the average shorter than the corresponding ones in the unstrained alloys. In order to understand the origin of these discrepancies, we calculated first-, second-, and third-shell interatomic distances in a tetragonally strained semiconductor alloy thin film, based on a model which combines the macroscopic theory of elasticity with the known structure of bulk pseudobinary alloys. The model is based on two assumptions: (1) the growth of the strained ternary layers is

pseudomorphic at all compositions, and (2) in the limit $x \rightarrow 0$, which implies negligible tetragonal distortion, the behavior of the ternary layer out of the plane of growth is identical to that of a bulk alloy.

The first assumption is reasonable as theoretical predictions for the critical thickness of an InAs layer epitaxially grown on InP vary between 20 and 40 Å.[46,47] This assumption allows one to predict first- (R_1), second- ($R_{2\parallel}$ and $R_{2\perp}$), and third- (R_3' and R_3'') shell distances for the limiting case corresponding to $x=1$, i.e., an InAs layer pseudomorphically grown on an InP substrate from the following formulas:

$$R_1(x=1)=\frac{a_{\mathrm{InP}}}{4}\sqrt{3+2\varepsilon_\perp+\varepsilon_\perp^2},$$

$$R_{2\parallel}(x=1)=\frac{a_{\mathrm{InP}}}{2}\sqrt{2} \quad \text{on epitaxial growth plane,}$$

$$R_{2\perp}(x=1)=\frac{a_{\mathrm{InP}}}{2}\sqrt{2+2\varepsilon_\perp+\varepsilon_\perp^2}$$

out of epitaxial growth plane, (4)

$$R_3'(x=1)=\frac{a_{\mathrm{InP}}}{4}\sqrt{11+2\varepsilon_\perp+\varepsilon_\perp^2}$$

closer to epitaxial growth plane,

$$R_3''(x=1)=\frac{a_{\mathrm{InP}}}{4}\sqrt{11+18\varepsilon_\perp+9\varepsilon_\perp^2}$$

further from expitaxial growth plane,

where $\varepsilon_\perp$ is obtained from macroscopic elasticity theory. We note that in this case of a binary layer different nearest-neighbor bond lengths are not allowed by symmetry.

The second assumption allows us to predict values in the other limiting case of an As impurity in InP (limit $x \rightarrow 0$); in fact in this case atoms on the plane of epitaxial growth, or close to it, are constrained by epitaxy to lie in the substrate's crystallographic positions, while atoms out of this plane are free to position themselves as in the case of unstrained bulk alloys at values given in Ref. 4 and in Fig. 7:

$$R_1(x\rightarrow 0)=R_1(x\rightarrow 0 \text{ in bulk}),$$

$$R_{2\parallel}(x\rightarrow 0)=\frac{a_{\mathrm{InP}}}{2}\sqrt{2} \quad \text{on epitaxial growth plane,}$$

$$R_{2\perp}(x\rightarrow 0)=R_2(x\rightarrow 0 \text{ in bulk})$$

out of epitaxial growth plane (alloy value), (5)

$$R_3'(x\rightarrow 0)=\frac{a_{\mathrm{InP}}}{4}\sqrt{11} \quad \text{closer to epitaxial growth plane,}$$

$$R_3''(x\rightarrow 0)=R_3(x\rightarrow 0 \text{ in bulk})$$

further from epitaxial growth plane (alloy value).

There are two distinct second- ($R_{2\parallel}$ and $R_{2\perp}$) and third-shell (R_3' and R_3'') distances in the $x \rightarrow 0$ limit; note also that $R_{2\perp}$ and R_3'' are therefore not obtained by substituting $\varepsilon_\perp=0$ in Eq. (4), which yields the bond distances in bulk InP, correct for the alloy only in the VCA. Moreover, in contrast to the VCA, the model predicts two different values for $R_{2\perp}$, relative to As-As and As-P bonds and two different values for R_3'' relative to As-In_{As} and As-In_P bonds may be extrapolated from the same theory.

The values of R_1, $R_{2\parallel}$, $R_{2\perp}$, R_3', and R_3'' for intermediate compositions were obtained by linearly extrapolating those for the two extreme compositions. This is an important assumption of our model. The measured second-shell interatomic distances $R^{(2)}_{\text{As-As}}$ and $R^{(2)}_{\text{As-P}}$ were compared to the following linear combination of $R_{2\parallel}$ and $R_{2\perp}$:

$$R_2=\frac{N_\perp R_{2\perp}+N_\parallel R_{2\parallel}}{N_\perp+N_\parallel}, \tag{6}$$

where $N_\perp$ and $N_\parallel$ are the effective coordination numbers, corrected for the polarization dependence and for the limited thickness (3 ML) of the ternary layers, as described above. As for the third shell, the measured $R^{(3)}_{\text{As-In}}$ was compared to weighted averages of R_3(As-In_P) and R_3(As-In_{As}). R_3(As-In_P) and R_3(As-In_{As}) were obtained from the corresponding R_3' and R_3'' values, with coefficients N' and N'' corrected for the polarization dependence and for the limited thickness of the layers.

The dashed lines in Figs. 8(a)–8(d) indicate the values of R_1, R_2, and R_3 predicted by this model. Our first-shell results are substantially compatible with both the model as well as the theory valid for the bulk alloys. We therefore cannot measure appreciable differences between the As-In nearest-neighbor bonds in the strained layers and in the unstrained alloys. However, it must be recalled [and can be seen in Fig. 8(a)] that differences in first-shell bond lengths induced exclusively from tetragonal strain are expected to be small (typically $\Delta R/R \approx 1\%$ for a tetragonal distortion value of $\varepsilon_\perp \approx 6\%$) and cannot be measured unless the error bars fall well below 0.01 Å. In the majority of cases, previous studies on epitaxial thin films report bond-length values which are within the error bar equal to values in unstrained alloys, both for group-IV (Refs. 14–16) and III-V-based systems.[10,17–19] However, variations of first-shell bond lengths due exclusively to tetragonal strain have been measured in some strained epitaxial films of III-V semiconductors.[6–9,12] We have verified that, in all cases, experimental determinations of first-shell bond lengths agree very well with the predictions of our model, which therefore places these results within a clear interpretative framework.

While for the first shell we are not able to appreciate significant deviations from the behavior of the unstrained alloys, clear differences appear in the comparison of the measured interatomic distances relative to the higher coordination shells. Here measured distances were on the average shorter than those found on bulk alloys, and in fairly good agreement with our model.

The effect on the second- and third-shell distances is primarily due to the tetragonal distortion of the unit cell: the observed contractions of $R^{(2)}_{\text{As-P}}$, $R^{(2)}_{\text{As-As}}$, and $R^{(3)}_{\text{As-In}}$ are a con-

sequence of the decrease of the average values of bond angles θ_{T2} and θ_{T3}, driven by the contraction of the corresponding in-plane values.

In Fig. 8(d), the measured values of $R^{(3)}_{\text{As-In}}$ are compared to two differently weighted averages of $R^{(3)}_{\text{As-In}_\text{P}}$ and $R^{(3)}_{\text{As-In}_\text{As}}$. Weights were calculated assuming a random distribution of As and P atoms on the mixed lattice (dashed line), and based on measured second-shell coordination numbers (dotted line). The former assumption appears to be valid for most of the superlattice samples, as explained further in this section, and fits the data very well.

The detailed comparison between experimental results and our model allows us to conclude that the differences in interatomic distances between the bulk alloys and the strained layers are mainly to be attributed to bond-angle adaptations, in analogy to the effect induced by alloying in bulk pseudobinary alloys. In both cases, the local adaptations to strain are clearly a direct consequence of the much lower-energy cost of bond bending relative to bond stretching in this system.[42] Similar conclusions were drawn for the Ge_xSi_{1-x}/Si(100) system[14] and for other III-V strained-layer systems,[7,10,18] based on the observation of almost constant first-shell bond lengths and lower signal intensities relative to higher coordination shells. However, we demonstrate this by performing a detailed structural investigation extended to the second and third coordination shells.

The best-fit values of second-shell As coordination, $N_{\text{As-As}}$, first- and third-shell MSRD, σ_1^2 and σ_3^2 and mean square angle fluctuations, σ_θ^2, are shown in Table II. Second-shell coordination numbers are consistent with a random distribution of As and P atoms on the chemically disordered lattice for samples H_3, H_5 and H_7, as has been found to be true for the unstrained samples. However, the local As coordination is found to be lower than expected for a random distribution in some samples, and in particular in sample H_1. Deviations from a random distribution in this sample also appear from the measured $R^{(3)}_{\text{As-In}}$ [see Fig. 8(d)]. Effects related to the limited thickness can account for a 20% reduction in As-As coordination in this sample. Ordering phenomena, by which an ordered In/P/In/As/In/P phase forms in the strained layer, as already observed in similar systems,[48–50] could explain a further decrease in second-shell As-As coordination. Finally, another possible cause could be related to the presence of three-dimensional $InAs_xP_{1-x}$ islands, as such a growth morphology would increase the relative number of As-P second-shell bonds. The latter possibility is realistic, as both HRXRD and HRTEM indicate a strong compositional degradation at the interfaces in this sample. A similar reduction in In-In second-shell coordination has been observed in 8 ML of InAs on GaAs, and has been associated to the presence of three-dimensional growth and to voids.[9]

First-shell mean-square relative displacement values are similar to those found for the bulk alloys. This finding is in agreement with similar results on the In-As bond in $InAs_xP_{1-x}$ strained layers[8,10] and in other systems of epitaxial layers of semiconductors.[18] Bond-angle fluctuations could be effectively estimated only for samples H_6 and H_7, and are similar to those found for the unstrained samples. For these samples the difference between in-plane and out-of-plane bond angles induced by a tetragonal distortion of the unit cell is expected to be $\geq 1°$, and is therefore within the error.

The present results on bond-angle distortions are quite different from the well-known bond-angle distortions found in amorphous tetrahedral semiconductors, such as amorphous Si, Ge, GaAs, and GeN.[51–54] In fact, in these systems the bond-angle distribution remains centered at 109.47°, and acquires a mean-square deviation of 6°–9°. Here the average value of bond angles shifts with increasing tetragonal strain, while the disorder remains virtually unchanged. In contrast to the first and second shells, third-shell mean-square relative displacement values are much larger than those found for the bulk alloys, indicating a general increase in static disorder with increasing distance from the central atom, to be attributed to the combined effect of alloying and tetragonal distortion.

VI. CONCLUSIONS

To conclude, interatomic distances relative to the first three coordination shells around As in thin strained $InAs_xP_{1-x}$ layers have been obtained by performing a complete MS analysis of the XAFS spectra. The comparison with unstrained alloys of similar composition shows that the amplitude of the distortions attributed to tetragonal strain is well reproduced by a model which combines macroscopic elasticity theory and the known structure of bulk pseudobinary alloys. The influence of tetragonal distortion on the local structure starts appearing in second- and third-shell distance values, indicating that the local adaptations to strain act mainly on bond angles. The set of structural parameters measured indicates that the local structure in the strained layers is very similar to that found in unstrained alloys on a nearest-neighbor level. As the distance from the central atom increases, disorder also increases due to bond-angle distortions induced both by the alloying effect and by tetragonal strain.

ACKNOWLEDGMENTS

GILDA is an Italian Collaborating Research Group beamline at the European Synchrotron Radiation Facility (Grenoble, France) jointly funded by CNR, INFM, and INFN. We are indebted to P. Pattison for the loan of the solid state Ge detector. We acknowledge excellent technical assistance of F. Campolungo, L. Sangiorgio, V. Sciarra, and V. Tullio (INFN, Frascati) in the design, construction, commissioning and operation phases of the GILDA beamline, and of R. Graziola and G. Chini (Università di Trento) in the setup of the experimental apparatus. We are indebted to all the III-V staff of CSELT laboratories (Torino) and in particular with G. M. Schiavini for the LP-MOCVD growths, and with L. Gastaldi, F. Taiariol, and D. Soldani for the HRXRD measurements, data elaboration and interpretation; interesting discussions with C. Papuzza, L. Lazzarini, C. Ferrari, and G. Salviati are also acknowledged. We acknowledge stimulating discussions on the GNXAS method with A. Filipponi.

*Mailing address: GILDA CRG, ESRF, BP 220, 38043 Grenoble Cedex, France.

[1] J. C. Mikkelsen and J. B. Boyce, Phys. Rev. Lett. **49**, 1412 (1982).
[2] A. Balzarotti, M. Czyzyk, A. Kisiel, N. Motta, M. Podgorny, and M. Zimnal-Starnawska, Phys. Rev. B **30**, 2295 (1984).
[3] J. L. Martins and A. Zunger, Phys. Rev. B **30**, 6217 (1984).
[4] Y. Cai and M. F. Thorpe, Phys. Rev. B **46**, 15 872 (1992); 15 879 (1992).
[5] O. Brandt, K. Ploog, R. Bierwolf, and M. Hohenstein, Phys. Rev. Lett. **68**, 1339 (1992).
[6] J. C. Woicik, J. G. Pellegrino, S. H. Southworth, P. S. Shaw, B. A. Karlin, C. E. Bouldin, and K. E. Miyano, Phys. Rev. B **52**, R2281 (1995).
[7] M. G. Proietti, S. Turchini, J. Garcia, G. Lamble, F. Martelli, and T. Prosperi, J. Appl. Phys. **78**, 6574 (1995).
[8] Y. Kuwahara, H. Oyanagi, R. Shioda, Y. Takeda, H. Yamaguchi, and M. Aono, Jpn. J. Appl. Phys. **33**, 5631 (1994).
[9] J. C. Woicik, K. E. Miyano, J. G. Pellegrino, P. S. Shaw, S. H. Southworth, and B. A. Karlin, Appl. Phys. Lett. **68**, 3010 (1996).
[10] C. Lamberti, S. Bordiga, F. Boscherini, S. Pascarelli, and G. M. Schiavini, Appl. Phys. Lett. **64**, 1430 (1994); C. Lamberti, S. Bordiga, F. Boscherini, S. Pascarelli, G. M. Schiavini, C. Ferrari, L. Lazzarini, and G. Salviati, J. Appl. Phys. **76**, 4581 (1994); F. Boscherini, S. Pascarelli, C. Lamberti, S. Bordiga, and G. M. Schiavini, Nucl. Instrum. Methods Phys. Res. B **97**, 23 (1995).
[11] H. Oyanagi, Y. Takeda, T. Matsushita, T. Ishiguro, T. Yao, and A. Sasaki, Superlatt. Microstruct. **4**, 413 (1988).
[12] M. Tabuchi, T. Kumamoto, and Y. Takeda, J. Appl. Phys. **77**, 143 (1995).
[13] J. C. Woicik, J. Phys. (France) IV (to be published).
[14] J. C. Woicik, C. E. Bouldin, M. I. Bell, J. O. Cross, D. T. Tweet, B. D. Swanson, T. M. Zhang, L. B. Sorensen, C. A. King, J. L. Hoyt, P. Pianetta, and J. F. Gibbons, Phys. Rev. B **43**, 2419 (1991).
[15] M. Matsuura, J. M. Tonnere, and G. S. Cargill III, Phys. Rev. B **44**, 3842 (1991).
[16] A. P. Hitchcock, J. Aubry, T. Tyliszczak, Z. H. Lu, J. M. Baribeau, and T. E. Jackman, J. Phys. (France) IV (to be published).
[17] Y. Takeda, H. Oyanagi, and A. Sasaki, J. Appl. Phys. **68**, 4513 (1990).
[18] S. C. Woronick, E. Canova, Y. H. Kao, M. E. Mills, T. W. Nee, and V. Rehn, J. Appl. Phys. **61**, 2836 (1987).
[19] M. G. Proietti, S. Turchini, F. Martelli, J. Garcia, and T. Prosperi, J. Appl. Phys. **77**, 62 (1995).
[20] C. Lamberti, Comput. Phys. Commun. **93**, 53 (1996); **93**, 82 (1996), and references therein.
[21] T. Wang, E. H. Reihlen, H. R. Jen, and G. B. Stringfellow, J. Appl. Phys. **66**, 5376 (1989).
[22] J. Hergeth, D. Grutzmacher, F. Reinhardt, and P. Balk, J. Cryst. Growth **107**, 537 (1991).
[23] F. Genova, A. Antolini, L. Francesio, G. Gastaldi, C. Lamberti, C. Papuzza, and C. Rigo, J. Cryst. Growth **120**, 333 (1992).
[24] A. Antolini, L. Francesio, L. Gastaldi, F. Genova, C. Lamberti, L. Lazzarini, C. Papuzza, C. Rigo, and G. Salviati, J. Cryst. Growth **127**, 189 (1993).
[25] R. Benzaquen, A. P. Roth, and R. Leonelli, J. Appl. Phys. **79**, 2640 (1996).
[26] M. Hybertsen, Phys. Rev. Lett. **64**, 555 (1990).
[27] J. S. Nelson, S. R. Kurtz, L. R. Dawson, and J. A. Lott, Appl. Phys. Lett. **57**, 578 (1990).
[28] M. Peressi, S. Baroni, A. Baldereschi, and R. Resta, Phys. Rev. B **41**, 12 106 (1990).
[29] A. A. Bonapasta and G. Scavia, Phys. Rev. B **50**, 2671 (1994).
[30] S. Pascarelli, F. D'Acapito, G. Antonioli, A. Balerna, F. Boscherini, R. Cimino, G. Dalba, P. Fornasini, G. Licheri, C. Meneghini, F. Rocca, and S. Mobilio, ESRF Newsletter **23**, 17 (1995).
[31] S. Pascarelli, F. Boscherini, F. D'Acapito, J. Hrdy, C. Meneghini, and S. Mobilio, J. Synchrotron Radiat. **3**, 147 (1996).
[32] S. Pascarelli, F. Boscherini, C. Lamberti, and S. Mobilio, J. Phys. (France) IV (to be published).
[33] F. Boscherini, S. Pascarelli, C. Lamberti, G. Gastaldi, R. De Martino, P. Calicchia, and F. Comin, J. Phys. (France) IV (to be published).
[34] A. Filipponi, A. Di Cicco, C. R. Natoli, Phys. Rev. B **52**, 15122 (1995); A. Filipponi and A. Di Cicco, *ibid.*, 15 135 (1995).
[35] A. Filipponi, J. Phys., Condens. Matter. **3**, 6489 (1991).
[36] M. Benfatto, C. R. Natoli, and A. Filipponi, Phys. Rev. B **40**, 9626 (1989).
[37] J. J. Boland, S. E. Crane, and J. D. Baldeschwieler, J. Chem. Phys. **77**, 142 (1982).
[38] O. Heckmann, H. Magnan, P. le Fevre, D. Chandesris, and J. J. Rehr, Surf. Sci. **312**, 62 (1994).
[39] P. A. Lee, P. H. Citrin, P. Eisenberger, and B. M. Kincaid, Rev. Mod. Phys. **53**, 769 (1981).
[40] J. C. Mikkelsen and J. B. Boyce, Phys. Rev. B **28**, 7130 (1983).
[41] P. Letardi, N. Motta, and A. Balzarotti, J. Phys. C **20**, 2853 (1987).
[42] R. M. Martin, Phys. Rev. B **1**, 4005 (1970).
[43] A. B. Chen and A. Sher, Phys. Rev. B **32**, 3695 (1985).
[44] C. K. Shih, W. E. Spicer, W. A. Harrison, and A. Sher, Phys. Rev. B **31**, 1139 (1985).
[45] Z. Wu, K. Lu, Y. Wang, J. Dang, H. Li, L. Li, and Z. Fang, Phys. Rev. B **30**, 8694 (1993).
[46] J. W. Matthews and A. E. Blakeslee, J. Cryst. Growth **27**, 118 (1974).
[47] R. People and J. C. Bean, Appl. Phys. Lett. **49**, 229 (1986).
[48] M. A. Shahid, S. Mahajan, and D. E. Laughlin, Phys. Rev. Lett. **58**, 2567 (1987).
[49] H. R. Jen, M. J. Cherng, and G. B. Stringfellow, Appl. Phys. Lett. **48**, 1603 (1986).
[50] T. S. Kuan, T. F. Kuech, W. I. Wang, and E. L. Wilkie, Phys. Rev. Lett. **54**, 201 (1985).
[51] C. E. Bouldin, R. A. Forman, and M. I. Bell, Phys. Rev. B **35**, 1429 (1987).
[52] L. Incoccia, S. Mobilio, M. G. Proietti, P. Fiorini, C. Giovannella, and F. Evangelisti, Phys. Rev. B **31**, 1028 (1985).
[53] F. Boscherini, A. Filipponi, S. Pascarelli, F. Evangelisti, S. Mobilio, F. C. Marques, and I. Chambouleyron, Phys. Rev. B **39**, 8364 (1989).
[54] F. Boscherini, in *Amorphous Silicon Technology-1992*, edited by M. J. Thompson, Y. Hamakawa, P. G. Le Comber, A. Madan, and G. A. Schiff, MRS Symposia Proceedings No. 258 (Materials Research Society, Pittsburgh, 1992), p. 217.